J Mater Sci (2007) 42:4609–4623
DOI 10.1007/s10853-006-0520-y

Micro-mechanics based derivation of the materials constitutive relations for carbon-nanotube reinforced poly-vinyl-ester-epoxy based composites

Mica Grujicic · D. C. Angstadt · Y. P. Sun · K. L. Koudela

Received: 18 April 2006 / Accepted: 6 June 2006 / Published online: 16 February 2007

Abstract The atomic-level computational results of the mechanical properties of Multi-Walled Carbon Nanotube (MWCNT) reinforced poly-vinyl-ester-epoxy obtained in our recent work [Grujicic M, Sun Y-P, Koudela KL (2006) Appl Surf Sci (accepted for publication, March)], have been utilized in the present work within a continuum-based micro-mechanics formulation to determine the effective macroscopic mechanical properties of these materials. Since the MWCNT reinforcements and the polymer-matrix molecules are of comparable length scales, the reinforcement/matrix interactions which control the matrix-to-reinforcement load transfer in these materials are accounted for through direct atomic-level modeling of the "*effective reinforcement*" mechanical properties. The term an "*effective reinforcement*" is used to denote a MWCNT surrounded by a layer of the polymer matrix whose thickness is comparable to the MWCNT radius and whose conformation is changed as a result of its interactions with the MWCNT. The micro-mechanics procedure yielded the effective continuum mechanical properties for the MWCNT-reinforced poly-vinyl-ester-epoxy matrix composite mats with a random in-plane orientation of the MWCNTs as a function of the following composite microstructural parameters: the volume fraction of the MWCNTs, their aspect ratio, the extent of covalent functionalization of the MWCNT outer walls as well as a function of the mechanical properties of the matrix and the reinforcements.

Introduction

Due to a perceived potential for large gains in mechanical and physical properties as compared to standard structural materials, nano-structured (in particular, carbon nanotube-reinforced polymer-matrix composite) materials have spurred considerable interest in the materials community. In other words, the exceptional physico-mechanical properties, high aspect ratio and low density of the single-walled carbon nanotubes (SWCNTs) and multi-walled carbon nanotubes (MWCNTs) have made them ideal mechanical reinforcement candidates for the next generation of polymer-based composites [1]. The elastic modulus as high as 1TPa and a tensile strength close to 60 GPa have been reported in SWCNTs. These values are five and at least thirty times greater than their respective counterparts in steels, and at only one sixth of the weight [2–5]. Thus, the SWCNTs appear to be ideal mechanical reinforcements for lightweight composite systems. However, the material and the processing cost for the SWCNTs, even when they are produced using large-scale high-yield

---

M. Grujicic (✉) · D. C. Angstadt
Department of Mechanical Engineering, Clemson University, 241 Engineering Innovation Building, Clemson, SC 29634-0921, USA
e-mail: mica.grujicic@ces.clemson.edu

Y. P. Sun
Department of Chemistry, Clemson University, Clemson, SC 29634, USA

K. L. Koudela
Applied Research Laboratory, Pennsylvania State University, 155, ARL Building, University Park, PA 16802, USA

technologies, are very high primarily due to the costly separation and non-destructive purification processing. Consequently, while the mechanical properties of MWCNTs are generally less attractive (the elastic modulus typically around 350 GPa and a tensile strength around 8 GPa) relative to those found in the SWCNTs, the lower-cost MWCNTs are currently being considered as a more realistic mechanical reinforcement candidate for the commercially viable polymer-matrix composites.

A number of experimental investigations reported in the literature established that the mechanical properties of both SWCNT- and MWCNT-reinforced polymer-matrix composites are significantly below their theoretically predicted potential [e.g., 6] and that they are controlled by the extent of dispersion of the nanotubes in the polymer matrix and by the nanotube/polymer interface bond strength [6–9]. The nanotube reinforcements are often found aggregated into bundles (ropes), weakly interacting via the van der Waals attractive forces [10, 11]. Such bundles can contain up to several hundred nanotubes arranged in a hexagonal lattice [10, 12]. The nanotubes within a bundle can easily slide relative to each other giving rise to a low value of the shear modulus of the carbon nanotube bundles [10]. As an example, the elastic modulus of the microscopic polymer-free SWCNT-based fibers and strands are found to be only 80 GPa [13] and 77 GPa [14], respectively. In addition to reducing the shear modulus, the nanotube aggregation gives rise to the undesirable reduction in the reinforcement aspect ratio.

Obtaining a homogeneous dispersion of the nanotubes in the polymer matrix is not easily accomplished for a number of reasons the primary one being very low solubility of the nanotube bundles in most solvents [15]. As far as the nanotube/polymer interfacial-bonding strength is concerned, its magnitude is believed to be limited by the atomically smooth, non-reactive nature of the nanotubes outer wall [1]. This, in turn, limits the load transfer from the polymer matrix to nanotubes which controls the extent of stiffening/strengthening induced by the nanotube reinforcements. To address these problems, several strategies for synthesis of the nanotube-reinforced polymer-matrix composites have been developed, including solution-casting with ultrasonication [16–21], melt-mixing [22, 23], surfactant-assisted processing [24], surface modification strategies (e.g., grafting and polymer wrapping) [25], and in-situ polymerization of monomers in the presence of carbon nanotubes [26, 27]. All these efforts/approaches have so far resulted in relatively modest improvements of the homogeneity of nanotubes distribution within the polymer matrix and of the nanotube/polymer interfacial bond strength.

The extremely small dimensions of the nanotubes (the diameter of a couple of nano-meters and the length of a few microns), present serious challenges for experimental characterization of nanotube-based reinforcement phenomena in the polymer-matrix composites. Macroscopic tensile tests used to study the elastic/plastic deformation and fracture behavior of the nanotubes-reinforced polymer-matrix composites suffer from a number of serious limitations, the two most important being: (a) insufficient load and displacement resolutions to capture the changes in stress/strain behavior at the micro and nano scales [28, 29] and (b) fabrication of the macroscopic tensile test specimens can often introduce surface flaws and, hence, undesirable stress concentrations [28, 29]. It is generally accepted that the nano-indentation and nano-scratch based experimental techniques combined with high-resolution imaging (e.g., electron microscopy) are currently the most reliable and accurate methods for studying and quantifying the effect of nanotubes on the deformation behavior of polymer-matrix composites [28, 29]. It is also generally recognized that atomic-level calculations based on the high-fidelity multi-body quantum-mechanics based forcefields to account for the inter- and intra-molecular atomic interactions is critical for obtaining a better understanding of the phenomena controlling the nature and the level of nanotube-induced stiffening/strengthening (e.g., interfacial bonding and matrix-to-reinforcement load transfer mechanisms) in polymer-matrix composites [e.g., 30, 31].

In our recent work [32], such atomic-level calculations were carried out to understand the role of sidewall functionalization of a model MWCNT (i.e., a (5,5) (10,10) (15,15)) three-walled carbon nanotube (3WCNT) in a vinyl-ester-epoxy polymer matrix on the matrix-to-reinforcement load transfer and on the resulting atomic level mechanical properties. It should be noted that while the sidewall functionalization can be achieved in many different covalent and non-covalent ways, covalent functionalization is generally believed to yield better load transfer between the matrix and the reinforcements (although such functionalization may promote matrix/reinforcement interfacial fracture through the introduction of defects in the outer wall of the nanotubes). On the other hand, when in addition to providing mechanical reinforcement to the polymer matrix, the nanotubes are required to retain their good electrical properties, functionalization of a non-covalent character should be chosen so that the electronic characteristics of the carbon nanotubes (governed by their sp^2 hybridization) are not altered. In our ongoing work [33] (the present paper is a part of the ongoing work), a new class of MWCNT-reinforced poly-vinyl-ester-epoxy based armor for mitigation of the effects of Improvised Explosive Devices (IEDs) is being developed. For such armor, a good load transfer between the polymer matrix and the nanotube reinforcements is important for its structural performance and its tendency for interfacial failure is critical for its energy-absorbing ballistic performance while no retention of the good electrical conductivity of the nanotubes is required. That is the reason why the role of covalent-type MWCNT-sidewall functionalization on the matrix-to-reinforcement load transfer has been investigated in the present work.

The atomic-level mechanical properties in 3WCNT-reinforced poly-vinyl-ester-epoxy obtained in our recent work [32] include, in an implicit manner, the atomic-microstructure dependent interfacial load transfer phenomena and the effect of the altered polymer matrix conformation in the region surrounding the reinforcement. These matrix reinforcement regions are found to be comparable in thickness with the reinforcement radius and are fully entangles with the surrounding polymer matrix ensuring a full load transfer. Hence, it appears justified to consider the resulting composite microstructure as consisting of continuum "*effective reinforcements*" embedded into and fully bonded with a bulk-like polymer matrix. The term "*effective reinforcements*" is used to denote the assembly of 3WCNTs and the surrounding interfacial polymer matrix, Fig. 1, where the mechanical properties of such reinforcements have been determined (as a function of sidewall covalent functionalization) in our recent work [32]. The objective of the present work is then to employ the existing continuum-based micro-mechanics models to determine the effective mechanical properties of 3WCNT-reinforced poly-vinyl-ester-epoxy as a function of the extent of covalent functionalization, 3WCNT aspect ratio, and reinforcement volume fraction. While the method used enables the determination of such properties for various spatial distributions of the reinforcements within the matrix; the method is applied only to the class of sheet-like 3WCNT-reinforced poly-vinyl-ester-epoxy mats in which well-dispersed nanotubes are parallel with the mat faces but have a random in-plane orientation. Such mats have been produced in our ongoing work [33] through a combination of nanotube-reinforced fiber spinning and fiber lay-out techniques. The resulting effective composite mechanical properties are cast into models directly suited for use in commercial finite-element structural and ballistic analysis computer programs.

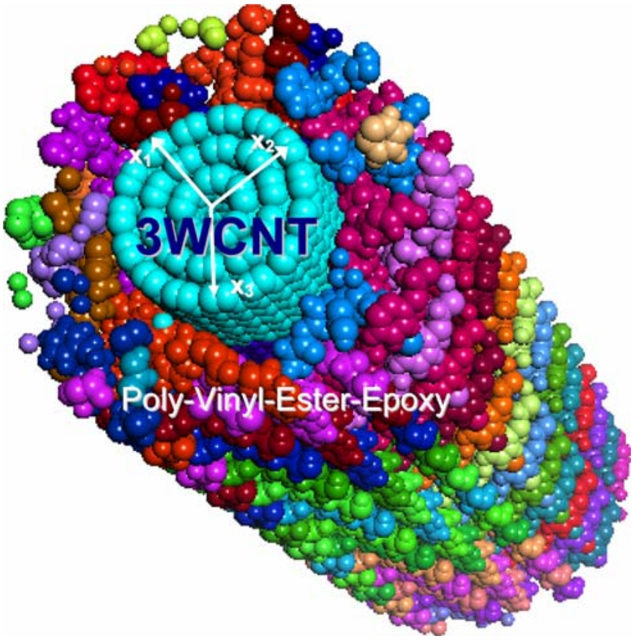

Fig. 1 Atomic structure of a short segment of the 3WCNT + surrounding poly-vinyl-ester-epoxy based effective reinforcement used in the present work

The organization of the paper is as follows: A detailed description of the derivations of the material models for the constituent materials (i.e., the 3WCNT-based effective reinforcements and the poly-vinyl-ester-epoxy matrix) and of the composite effective mechanical properties are presented in sections "Mechanical properties of the constituent materials" and "Micro-mechanics based analysis of composite effective mechanical properties," respectively. The main results pertaining to the ballistic performance of an armor made of the 3WCNT-reinforced poly-vinyl-ester-epoxy matrix composite obtained in the present work are presented and discussed in section "Testing of the present model," while the key conclusions resulted from the present study are summarized in section "Summary and conclusions."

Computational procedure

Mechanical properties of the constituent materials

In this section, a brief overview is given of the basic mechanical properties of the two constituent materials: the 3WCNT-based effective reinforcements and the vinyl-ester-epoxy polymer matrix.

3WCNT-based effective reinforcements

The analysis carried out in our recent work [32] clearly established that the 3WCNT-based effective reinforcements are transversely isotropic materials with the plane of isotropy being normal to the nanotube-reinforcement axis. Within a reinforcement-based local coordinate system in which the x_1 axis is aligned with the reinforcement axis, the linear elastic stiffness matrix is defined in terms of five independent stiffness components (C_{11}, C_{22}, C_{12}, C_{23}, and C_{44}). The values of these constants are found to be (at least initially) linearly dependent on the extent of sidewall covalent functionalization of the 3WCNTs. A summary of the elastic stiffness properties as a function of the degree of sidewall functionalization of the 3WCNTs is given in Table 1.

As far as the yield behavior of the effective reinforcement is considered, it is found to be governed by a six-coefficient parabolic yield function in the form:

$$a_{11}\sigma_{11}^2 + a_{22}\left(\sigma_{22}^2 + \sigma_{33}^2\right) + 2a_{12}(\sigma_{11}\sigma_{22} + \sigma_{11}\sigma_{33}) + 2a_{23}\sigma_{22}\sigma_{33} + 2a_{44}\sigma_{23}^2 + 2a_{66}\left(\sigma_{31}^2 + \sigma_{12}^2\right) = R \qquad (1)$$

where a's and R are yield-function coefficients (one of these is not independent) and σ's are the stress components.

Table 1 The effect of sidewall covalent functionalization on the linear elastic stiffness coefficients for the 3WCNT-based effective reinforcements[a]

Elastic constant	Unit	Functionalization dependent value
C_{11}	GPa	282.3 + 10.40p[b]
C_{22}	GPa	269.3 + 73.17p
C_{12}	GPa	59.60 + 2.196p
C_{23}	GPa	271.2 + 82.29p
C_{44}	GPa	3.840 + 0.485p

[a] Reinforcement axis is along the x_1 coordinate axis

[b] p = percent of the outer wall 3WCNT sites covalently functionalized

The values of the coefficients appearing in Eq. 1, as a function of the degree of sidewall functionalization of the 3WCNTs, are listed in Table 2. As seen in Table 2, the effective-reinforcement material displays a linear strain-hardening behavior since the square root of the coefficient R (which scales with the flow stress) is a linear function of the equivalent plastic strain, ε_{pl}.

The failure behavior of the 3WCNT-based effective reinforcement is defined using an orthotropic damage model. Within this model, the failure initiation is stress-based and occurs when the magnitude of a stress component σ_{ij} reaches a critical value, σ_{ij}^*. The values of the critical stress components, as determined in our previous work [32], are listed in Table 3. The failure initiation criteria mentioned above defines a surface of valid stresses. If a state of stress is found to lie outside of this surface during loading, a backward-Euler algorithm is used to return the stress to the failure surface. The resulting inelastic incremental strain is accumulated and generally referred to as a "*cracked strain*," ε_{cr}. This causes a reduction in the maximum stress that the material can support, i.e. strain softening. The energy absorbed by the material during post-initiation failure is proportional to the corresponding material fracture energy, G_{ij}, where the subscripts i and j denote the orientation of the crack surfaces and the mode (normal versus shear) of loading, respectively. Thus a full definition of the orthotropic damage model used in the present work entails the knowledge of the six critical failure-initiation stress components and the six post failure-initiation fracture energies. The values of the fracture energies, as determined in our previous work [32], are listed in Table 3.

The post-initiation strain-softening behavior described above is typically approximated using a linear damage model within which the critical failure-

Table 2 The effect of sidewall covalent functionalization on the quadratic yield function coefficients for the 3WCNT-based effective reinforcements[a]

Coefficient	Unit	Functionalization dependent value
a_{11}	N/A	0.0015133 + 0.00023667p[b]
$a_{22} = a_{33}$	N/A	0.66667
$a_{12} = a_{13}$	N/A	–0.45333 – 0.01333p
a_{23}	N/A	–0.17333 + 0.013333p
a_{44}	N/A	1.5667 – 0.066667p
$a_{55} = a_{66}$	N/A	0.9507 + 0.004333p
R	MPa^2	$(1944.0 + 403.71p)(1 + 4.67\bar{\varepsilon}_{\mathrm{pl}})^2$

[a] Reinforcement axis is along the x_1 coordinate axis

[b] p = percent of the outer wall 3WCNT sites covalently functionalized

Table 3 The effect of sidewall covalent functionalization on the failure parameters for the 3WCNT-based effective reinforcements[a]

Parameter	Symbol	Unit	Functionalization dependent value
Failure stress	σ^*_{11}	MPa	1,168.6 + 4.545p *
Failure stress	σ^*_{22}	MPa	52.100 + 2.511p
Failure stress	σ^*_{33}	MPa	52.100 + 2.511p
Failure stress	σ^*_{12}	MPa	30.899 + 0.893p
Failure stress	σ^*_{23}	MPa	30.080 + 1.443p
Failure stress	σ^*_{31}	MPa	30.899 + 0.893p
Fracture energy	G_{11}	J/m^2	292.01 + 1.89p
Fracture energy	G_{22}	J/m^2	65.125 + 0.393p
Fracture energy	G_{33}	J/m^2	65.125 + 0.393p
Fracture energy	G_{12}	J/m^2	68.73 + 1.94p
Fracture energy	G_{23}	J/m^2	67.68 + 2.03p
Fracture energy	G_{31}	J/m^2	68.73 + 1.94p

[a] Reinforcement axis is along the x_1 coordinate axis

[b] p = percent of the outer wall 3WCNT sites covalently functionalized

stress components decrease linearly with the corresponding component of the cracked strain. A complete failure for a given mode of loading occurs when the corresponding crack strain reaches a critical value. The critical crack-strain values scale with the corresponding fracture energies and are inversely proportional to the corresponding critical failure-initiation stresses. The extent of post failure-initiation damage associated with a given mode of loading, D_{ij}, is defined as the ratio of the corresponding current crack strain and the corresponding maximum crack strain. Thus, the extent of damage is zero at the point of failure initiation and is equal to one at the point when the material completely loses the ability to support the given type of load. Furthermore, the post-initiation critical failure stress associated with a given mode of loading decreases at a rate of (1–D_{ij}) from its maximum failure-initiation value. A complete loss of the load carrying capacity for multi-axial loading then is defined by the following criterion:

$$\left(\frac{\sigma_{11}}{\sigma^*_{11}(1-D_{11})}\right)^2+\left(\frac{\sigma_{22}}{\sigma^*_{22}(1-D_{22})}\right)^2+\left(\frac{\sigma_{33}}{\sigma^*_{33}(1-D_{33})}\right)^2+\left(\frac{\sigma_{12}}{\sigma^*_{12}(1-D_{12})}\right)^2 +\left(\frac{\sigma_{23}}{\sigma^*_{23}(1-D_{23})}\right)^2+\left(\frac{\sigma_{31}}{\sigma^*_{31}(1-D_{31})}\right)^2\geq 1 \tag{2}$$

Vinyl-ester-epoxy polymer matrix

The poly-vinyl-ester-epoxy matrix is treated as follows

(a) A linear-elastic isotropic material with the weakly (and hence assumed non) rate-dependent elastic modulus E = 2.9 GPa and the Poisson's ratio v = 0.39 [34];

(b) The isothermal isotropic yield behavior of this material is taken to be governed by the von-Misses J_2 criterion. While the yield stress σ_y and the isotropic work-hardening rate h of this material are deformation-rate dependent, only their high deformation-rate values are used and the overall yield behavior assumed to be rate-independent. This can be justified by the fact that the main intended use of the present material model for the MWCNT-reinforced poly-vinyl-ester-epoxy is in the simulations of the ballistic performance of armor where the attendant deformation rates are quite high. The yield behavior of the poly-vinyl-ester-epoxy has also been expressed using the six-coefficient parabolic yield function, Eq. 1, except for the following conditions $a_{11} = a_{22} = a_{33} = 2/3$, $a_{12} = a_{23} = a_{31} = -1/3$, $a_{44} = a_{55} = a_{66} = 1$, and $R = 2/3\sigma^2_{\text{flow}}$ where the flow stress, $\sigma_{\text{flow}} = \sigma_y + h\bar{\varepsilon}_{\text{pl}}$, ($\bar{\varepsilon}_{\text{pl}}$ is the equivalent plastic strain) and

(c) Failure of the poly-vinyl-ester-epoxy matrix is taken to occur at an equivalent plastic-strain level of $\bar{\varepsilon}_{\text{pl}} = 0.045$ and to be associated with a fracture energy level of G = 96 J/m^2 [35].

A summary of the mechanical properties of the vinyl-ester-epoxy polymer matrix is given in Table 4.

Micro-mechanics based analysis of composite effective mechanical properties

In this section, the mechanical properties of the two constituent materials (the effective 3WCNT-reinforcements and the poly-vinyl-ester-epoxy) are

Table 4 Stiffness, yield and failure properties of the poly-vinyl-ester-epoxy

Property	Symbol	Unit	Value
Young's Modulus	E	GPa	2.9
Poisson's ratio	v	N/A	0.39
Yield stress	σ_y	MPa	52
Tangent Modulus	h	MPa	21
Failure strain	$\varepsilon_{\text{fail}}$	N/A	0.045
Fracture energy	G	J/m^2	96

utilized within a micromechanics based frame work to determine the effective mechanical properties of the 3WCNT-reinforced poly-vinyl-ester-epoxy based composite materials.

Elastic properties

The effective linear elastic properties of the composite material at hand are determined using the Mori–Tanaka micromechanics elastic-inhomogeniety method [36–39]. According to this method, the complete elastic stiffness tensor of a transversely-isotropic composite material is defined as:

$$C = C^m + v_f\left\langle\left(C^f - C^m\right)A^f\right\rangle\left(v_m I + v_f\left\langle A^f\right\rangle\right)^{-1} \tag{3}$$

where v_f and v_m are the reinforcement and the matrix volume fractions, respectively. I is the identity tensor, C^m is the stiffness tensor of the matrix material, C^f is the stiffness matrix of the reinforcement material and A^f is the reinforcement dilute mechanical strain-concentration tensor defined as:

$$A^f = \left[I + S(C^m)^{-1}\left(C^f - C^m\right)\right]^{-1} \tag{4}$$

where S is the Eshelby tensor [40]. The angle brackets ($\langle\ldots\rangle$) in Eq. 3 are used to represent the average value of the respective quantities over all reinforcement orientations after the quantities are expressed within the global (composite) coordinate system (x_1''', x_2''', x_3''') using the proper transformation from the local (reinforcement) coordinate system (x_1, x_2, x_3). For example, the dilute mechanical strain-concentration tensor for a reinforcement A^f after transformation to the global coordinate system is given as:

$$\bar{A}^f_{ijkl} = c_{ip}c_{jq}c_{kr}c_{ls}A^f_{pqrs} \tag{5}$$

where c_{ij}'s are the direction cosines for the local-to-global coordinate transformation which are expressed in terms of the appropriate Euler angles φ, γ and ψ (defined in Fig. 2) as:

$$c_{11} = \cos\phi\cos\psi - \sin\phi\cos\gamma\sin\psi \tag{6}$$

$$c_{12} = \sin\phi\cos\psi + \cos\phi\cos\gamma\sin\psi \tag{7}$$

$$c_{13} = \sin\psi\sin\gamma \tag{8}$$

$$c_{21} = -\cos\phi\sin\psi - \sin\phi\cos\gamma\cos\psi \tag{9}$$

$$c_{22} = -\sin\phi\sin\psi + \cos\phi\cos\gamma\cos\psi \tag{10}$$

$$c_{23} = \sin\gamma\cos\psi \tag{11}$$

$$c_{31} = \sin\phi\sin\gamma \tag{12}$$

$$c_{32} = -\cos\phi\sin\gamma \tag{13}$$

$$c_{13} = \cos\gamma \tag{14}$$

The dilute mechanical-strain tensor expressed in the global coordinate system and averaged over all reinforcement orientations is then given as [41]:

$$\left\langle\bar{A}^f\right\rangle = \frac{\int_{-\pi}^{\pi}\int_{0}^{\pi}\int_{0}^{\frac{\pi}{2}} \bar{A}^f(\phi,\psi,\gamma)\ \lambda(\phi,\psi)\ \sin(\gamma)d\phi d\gamma d\psi}{\int_{-\pi}^{\pi}\int_{0}^{\pi}\int_{0}^{\frac{\pi}{2}} \lambda(\phi,\psi)\ \sin(\gamma)d\phi d\gamma d\psi} \tag{15}$$

where λ (φ, ψ) is the orientation distribution function defined as

$$\lambda(\phi,\psi) = \exp[-s_1\phi^2]\exp[-s_2\psi^2] \tag{16}$$

and where the factors s_1 and s_2 control the orientation distribution function. Three cases of the orientation distribution function most frequently encountered are

$$\text{Random:} s_1 = 0,\ s_2 = 0\ \lambda(\phi,\psi) = 1 \tag{17}$$

$$\text{Aligned:} s_1 = \infty,\ s_2 = \infty\ \lambda(\phi,\psi) = \delta(\phi - 0)\delta(\psi - 0) \tag{18}$$

$$\begin{aligned}\text{Axisymmetric:} s_1 = k,\ s_2 = \infty\ \lambda(\phi,\psi)\\ = \exp[-k\phi^2]\delta(\psi - 0)\end{aligned} \tag{19}$$

where $\delta(y - \bar{y})$ is the Dirac's delta function, centered at $\bar{y}$. The "*random*" case refers to a three dimensional random orientation of the reinforcements which gives rise to an isotropic response of the material. The "*aligned*" case corresponds to perfectly aligned reinforcements along the x_1''' global-coordinate axis. It should be noted that the constant k describes the relative amount of alignment of the reinforcements with respect to the x_1''' axis. For large values of k ($k \to \infty$), the axisymmetric case approaches the aligned case, while for small values of k ($k \to 0$), the reinforcements are axisymmetrically distributed over all values of angle φ (i.e., randomly oriented) with respect to the x_1''' axis.

In the present work, the reinforcements are assumed to lie in an x_1'''–x_2''' plane (the plane parallel to the mat surfaces) and to be randomly distributed in such a plane (a transversely isotropic orientation of the reinforcements). For such a distribution function $\gamma = 0$, $\psi = 0$ and $0 \le \varphi \le \pi$, $\lambda(\varphi) = 1$ and the direction cosines given by Eqs. 6–14 define a simple rotational matrix about the local x_3-axis by a rotation angle φ. It

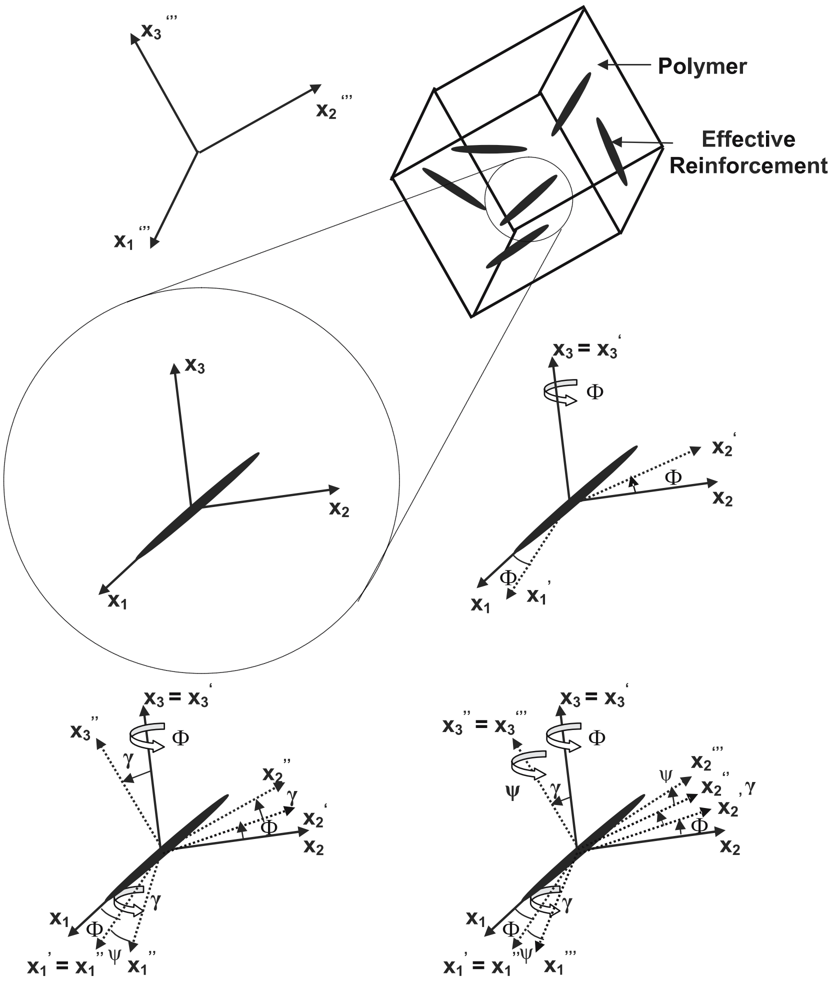

Fig. 2 Orientation relationship between the local reinforcement-based coordinate system x_1–x_2–x_3 and the global composite-based x_1'''–x_2'''–x_3''' coordinate system

should be recalled that the axis of the effective reinforcements is aligned in the local x_1 direction, while the composite material surfaces are normal to the global x_3''' axis and the reinforcements are located in the global x_1'''–x_2''' plane.

The effective elastic stiffness components of the 3WCNT-reinforced poly-vinyl-ester-epoxy matrix composite at given volume fractions and elastic properties of the two constituent materials, a specified reinforcement aspect ratio, a defined extent of sidewall functionalization of the 3WCNTs and for the transversely-isotropic distribution of the reinforcements are computed using Eqs. 3–15. When calculating the Eshelby tensor in Eq. 4, the cylinder-like effective reinforcements were assumed to have a prolate spheroidal geometry with a large aspect ratio.

Yield behavior

The load applied on a composite material is partitioned between its constituents (the reinforcements and the matrix). The onset of plasticity (or fracture) in the composite material then takes place when the general yield (or fracture) occurs in one of its constituents. There are many models in the literature which deal with the assessment of the effective strength and fracture properties of composite materials in terms of the properties of the constituent materials, composite architecture/microstructure, reinforcement/matrix interfacial bond strength and the dimensional scale. All these assessments fall within a property range. The upper bound of such a range for strength is defined by a simple rule of mixtures [34]. The lower bound is generally dependent on the composite architecture/microstructure and the reinforcement/matrix interfacial bond strength. In the present work, the following conservative estimate for the lower-bound composite strength consistent with the requirements for a continuous, ductile, matrix containing strong reinforcements and a perfect reinforcement/matrix bonding is used:

$$\sigma_y = \sigma_{y,m}\left[1 + \frac{1}{16}\left(\frac{v_F^{\frac{1}{2}}}{1 - v_F^{\frac{1}{2}}}\right)\right] \tag{20}$$

where σ_y and $\sigma_{y,\ m}$ denote the composite and the matrix yield/flow stresses, respectively. As explained earlier, since the polymer material within the effective reinforcements which surrounds the 3WCNT is fully entangled with the matrix polymeric material, the assumption regarding a perfect reinforcement/matrix bonding appears justified.

Since the plastic flow behaviors of both the 3WCNT-reiforcements and the matrix were defined in the previous two sections using a six-parameter parabolic yield function, Eq. 1, an attempt is made here to extend this approach to the composite material. This was done using the following steps:

(a) First, the parabolic yield-function constants a_{ij}'s for isolated effective reinforcements (aligned in the local x_1-direction) are used to compute the corresponding constants a_{ij}'s for the matrix-free 3WCNT-based mats in which the reinforcements are distributed randomly within a global x_1'''–x_2''' plane (Fig. 3) as:

$$a_{11}^* = \frac{a_{11} + a_{22}}{2} = a_{22}^* \tag{21}$$

$$a_{33}^* = a_{22} \tag{22}$$

$$a_{12}^* = \frac{a_{12} + a_{23}}{2} \tag{23}$$

$$a_{23}^* = a_{31}^* = a_{12} \tag{24}$$

$$a_{44}^* = a_{55}^* = \frac{a_{44} + a_{66}}{2} \tag{25}$$

$$a_{66}^* = a_{44} \tag{26}$$

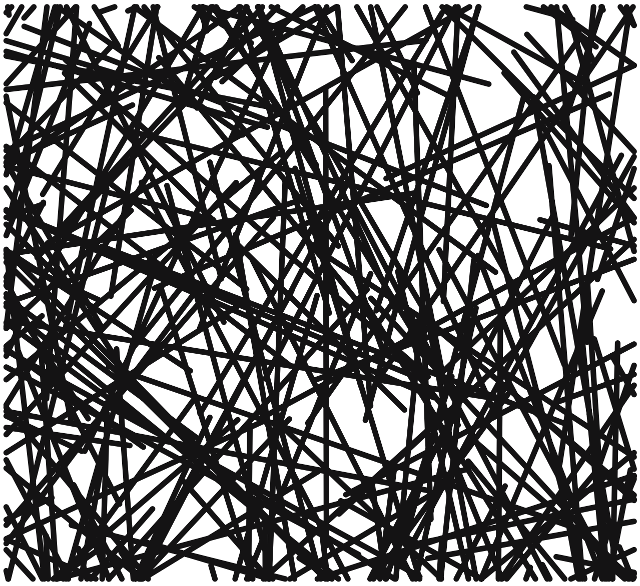

Fig. 3 A schematic of the matrix-free 3WCNT-based mat

where the values of a_{ij}'s appearing on the right hand side of Eqs. 21–26 are given in Table 2 and the values of these coefficients for the matrix-free mats is given in Table 5. The matrix-free 3WCNT-based yield function is then defined as:

$$\begin{aligned} & a_{11}^*\left(\sigma_{11}^2 + \sigma_{22}^2\right) + a_{33}^*\sigma_{33}^2 + 2a_{12}^*\sigma_{11}\sigma_{22} \\ & \quad + 2a_{23}^*(\sigma_{11}\sigma_{33} + \sigma_{22}\sigma_{33}) + 2a_{44}^*\left(\sigma_{23}^2 + \sigma_{31}^2\right) \\ & \quad + 2a_{66}^*\sigma_{12}^2 = R = \tfrac{2}{3}\sigma_y^2 \end{aligned} \tag{26}$$

(b) The a_{ij} yield-function coefficients for the composite material are then defined using the rule of mixtures and the corresponding values for these coefficients for the two constituent materials. As far as the coefficient $R = \frac{2}{3}\sigma_y^2$ is concerned, it is defined using the lower-bound estimate for the composite yield/flow stress, σ_y, Eq. 20. It should be noted that this approach correctly predicts that in the case of through-the-thickness uniaxial loading (only σ_{33} non-zero), plastic yielding occurs at a stress level equal to the matrix yield stress modified by the plastic constraining effect of the reinforcements (the lower bound value), as defined by Eq. 20.

Failure behavior

Our previous simulation work [32] clearly established that the onset of failure in 3WCNT-based effective reinforcements initiates at the SWCNT/polymer interface and that it is stress controlled. A preliminary atomic-level calculation [33] of the mechanical response of a single effective reinforcement embedded into the poly-vinyl-ester epoxy matrix suggests that the onset of failure in such composite material also takes place at the 3WCNT/polymer interface and that the stress-based failure-onset criterion can also be applied to the composite material as a whole. However, since the effective reinforcements carry a larger portion of

Table 5 The effect of sidewall covalent functionalization on the quadratic yield function coefficients for the matrix-free 3WCNT-based mats[a]

Coefficient	Unit	Functionalization dependent value[b]
$a_{11}^* = a_{22}^*$	N/A	$0.33410 + 0.00011830p$
a_{33}^*	N/A	0.66667
a_{12}^*	N/A	-0.31333
$a_{23}^* = a_{13}^*$	N/A	$-0.45333 - 0.01333p$
$a_{44}^* = a_{55}^*$	N/A	$1.2587 - 0.031167p$
a_{66}^*	N/A	$1.5667 - 0.066667p$
R	MPa^2	N/A

[a] Mat faces normal is along the x_1 coordinate axis

[b] p = percent of the outer wall 3WCNT sites covalently functionalized

the load in the composite material, the values of failure stresses, σ^*_{11}, σ^*_{22}, etc. in Table. 3, are re-evaluated for the composite material using a rule of mixtures approach with the (isotropic) failure stress for the matrix equal to its flow stress at the failure strain, $\varepsilon_{\mathrm{fail}} = 0.045$. As far as the fracture energy components of the composite material are concerned, they were also assumed to be given by a rule of mixtures and the isotropic fracture energy of the poly-vinyl-ester-epoxy matrix. This assumption appears justified by the fact that due to a discontinuous nature of the reinforcement phase and its small size, the cracks (while initiated at the nanotube/polymer interfaces) have to propagate through the matrix before the final failure of the composite material takes place.

Equation of state

In addition to the stiffness, strength, and failure equations defined in the previous sections, a complete ballistic material model requires specification of an equation of state. An equation of state defines a functional relationship between pressure, P, mass-density, ρ (specific volume, v) and internal energy density, e (temperature, T). A derivation of the equation of state for a transversely orthotropic material with the $x'''_1 - x'''_2$ plane of symmetry was reviewed in our recent work [32] and yielded:

$$\begin{aligned} P = &-\frac{1}{9}[2C_{11} + C_{33} + 2(C_{12} + 2C_{13})]\varepsilon_{\mathrm{vol}} \\ &-\frac{1}{3}(C_{11} + C_{12} + C_{13})(\varepsilon^d_{11} + \varepsilon^d_{22}) \\ &-\frac{1}{3}(2C_{13} + C_{33})\varepsilon^d_{33} \end{aligned} \tag{27}$$

The first term on the right hand side of Eq. 27 represents the standard linear relationship between the pressure and volumetric strain, $\varepsilon_{\mathrm{vol}}$, while the remaining terms on the right hand side of the same equation account for the coupling between the pressure and the deviatoric strain, ε^d_{ij}. The later terms of Eq. 27 are absent in the case of isotropic materials. The constant part of the first term on the right hand side of Eq. 27 represents the effective bulk modulus of the material, K. Under high strain-rate ballistic loading conditions, the relationship between the pressure and the volumetric strain is typically non-linear and, consequently, the first term on the right hand side of Eq. 27 is replaced by a non-linear relationship between the pressure and volumetric strain. Usually, the Mie–Gruneisen [42] equation of state is used to represent the first term on the right hand side of Eq. 27.

The Mie–Gruneisen equation of state defines the effect of current material mass density, ρ, and internal energy density, e, on pressure, P, as:

$$P = P_H + \Gamma\rho[e - e_H] \tag{28}$$

where the reference material states denoted by a subscript H correspond to the Hugoniot shock states of the material. These reference states are obtained by solving a system of simultaneous algebraic equations defining, for a stationary shock, the mass conservation, the momentum conservation and the energy conservation and a linear relationship between the shock speed, u_s and the particle velocity u_p, $u_s = c_0 + su_p$. The constants c_0 and s represent, respectively the bulk sound speed and a rate constant in the material. The bulk sound speed c_0 is given by:

$$c_0 = \sqrt{\frac{K}{\rho}} \tag{29}$$

where K is the effective bulk modulus of the material, defined in Eq. 27, and ρ is the current material mass density. The values for c_0 for the composite material at hand is calculated using Eq. 29 while the value for s was taken for the carbon-fiber reinforced epoxy polymer-matrix composite from the AUTODYN material database [43].

The Hugoniot quantities appearing in Eq. 28 are then computed as:

$$P_H = \frac{\rho_0 c_0^2 \mu(1 + \mu)}{[1 - (s - 1)\mu]^2} \tag{30}$$

and

$$e_H = \frac{1}{2}\frac{P_H}{\rho_0}\left(\frac{\mu}{1 + \mu}\right) \tag{31}$$

where ρ_0 denotes the initial (reference) material density.

The parameter Γ appearing in Eq. 28 (the Gruneisen Gamma) is a known thermodynamic material property and is defined as: $\Gamma(v) \equiv v(\partial P/\partial e)_v$. Gruneisen gamma allows the determination of thermodynamic states away from the reference Hugoniot states. Using the Maxwell-type state-property thermodynamic relations resulting from the Debye model for solids, the Gruneisen Gamma can be expressed as a function of the linear thermal expansion coefficient, α, the bulk modulus, K, the constant-volume specific heat, C_v and the density, ρ, as:

$$\Gamma \equiv \frac{3\alpha K}{\rho C_V} \tag{32}$$

Equation 32 and the rule-of-mixtures based values for the linear thermal expansion coefficient, the bulk modulus, the constant-volume specific heat, and the density are then used to compute the Gruneisen Gamma for the composite material at hand.

Testing of the present model

While the main objective of the present work was to carry out and report a detailed derivation of a ballistic material model for 3WCNT-reinforced poly-vinyl-ester-epoxy matrix composites the results of a few computational analyses of the ballistic performance of this material will be reported in this section in order to reveal the role of the basic material, architectural/microstructural and interfacial parameters. A detailed study of the ballistic performance of the composite material at hand will be reported in a companion paper [44]. All the calculations discussed in this section were carried out using AUTODYN a general-purpose non-linear dynamics computer program [43].

Problem definition

In the present work, a transient non-linear dynamics analysis of the impact and penetration of 3WCNT-reinforced poly-vinyl-ester-epoxy matrix composite armor by a *Fragment Simulating Projectile* (FSP) is carried out in order to determine the ballistic performance and the protection potential of the armor. The work was limited to the case of a normal impact of the armor by the FSP and, due to the axisymmetric nature of the problem, all the calculations are carried out using a two-dimensional (axisymmetric) model. A simple schematic of the projectile/armor impact/penetration problem analyzed here is given in Fig. 4. The projectile is cylindrical in shape with a diameter of 12.7 mm and a height of 12.7 mm. A constant initial normal velocity of 600 m/s is assigned to the projectile made of AISI 4340 steel and thus the initial kinetic energy of the projectile is approximately 2.3 kJ. A fixed thickness of 25.4 mm and a fixed lateral dimension of 100 mm for the armor are used for all the cases analyzed.

The interaction between the projectile and the armor is accounted for using the part-coupling option available in AUTODYN [43]. Except for the projectile/armor contact surfaces, zero-stress boundary conditions are prescribed on all faces of the projectile and the armor. All the calculations are carried out using the Lagrange processor for both the projectile and the armor. The projectile is represented using a mesh consisting of 900 rectangular cells. A mesh consisting of 3,000 rectangular cells is used to represent the armor. To improve the accuracy of the analysis, smaller cells are used in the regions of the projectile and the armor involved in the projectile/armor interactions. The computational mesh used is depicted in Fig. 5. It should be noted that the axis of symmetry in Fig. 5 is aligned with the left edge of the computational domain. A standard mesh sensitivity analysis is carried out in order to ensure that the results obtained are insensitive to the size of the cells used.

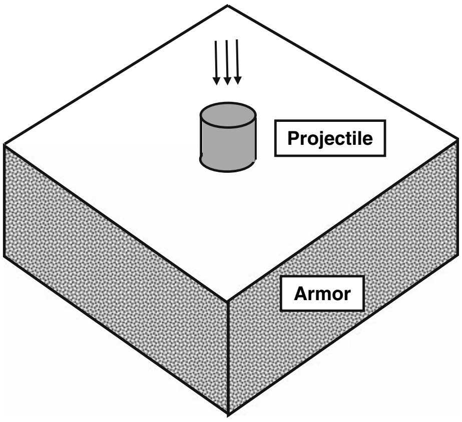

Fig. 4 A schematic of the projectile/armor impact analyzed in the present work

The ballistic performance of armor is quantified by a fraction of the initial kinetic energy of the projectile which has been absorbed by the armor or by impact-induced plastic deformation of the projectile. This quantity is referred to as the "*kinetic energy fraction absorbed*" in the remainder of the paper.

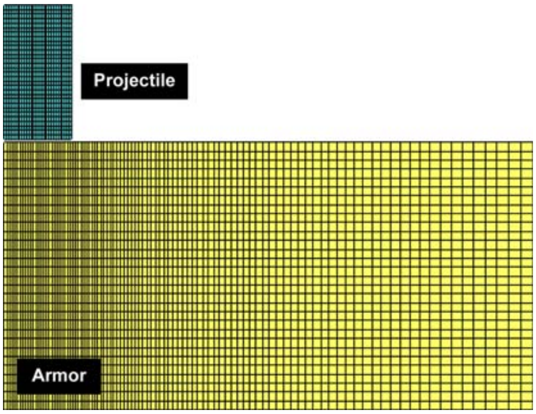

Fig. 5 The computational model of the projectile/armor impact analyzed in the present work

The effect of the following main 3WCNT-reinforced poly-vinyl-ester-epoxy matrix composite material parameters on the ballistic performance of the armor are examined in the next three sections: the 3WCNT-reinforcement length (i.e., the nanotube aspect ratio), the volume fraction of the reinforcement phase and the extent of side-wall covalent functionalization of the 3WCNT reinforcements.

A typical distribution of the damage/failure modes in the FSP and in the armor obtained in the present work is displayed in Fig. 6. The main damage/failure modes observed include plastic deformation, reinforcement breakage, reinforcement pull-out from the matrix and tensile failure on planes parallel with the armor faces (“*delamination*”). A more comprehensive discussion of these damage/failure modes will be presented in our future correspondence [44].

The effect of the 3WCNT length/aspect ratio

It is well-established that the extent of the matrix-to-reinforcement load transfer increases with the length (i.e., the aspect ratio) of the reinforcements giving rise to an enhanced stiffness of the composite material. The micro-mechanics based model utilized in the present work takes full account of this effect. Unfortunately, our atomistic calculations carried out in Ref. [32] were based on a short segment of the 3WCNT and, hence, the effect of the reinforcement length on the strength and the fracture properties could not be determined. Consequently, any effect of an increased 3WCNT length on the ballistic performance of the armor observed in the present work should be attributed solely to the attendant increase in the composite-material stiffness.

In this section, the effect of 3WCNT-reinforcement length on the ballistic performance of 3WCNT-reinforced poly-vinyl-ester-epoxy armor is examined. The respective results at two levels (0.1 and 0.2) of the 3WCNT-reinforcement volume fraction (defined in the next section) in the case of non-functionalized 3WCNTs are displayed in Fig. 7a. The corresponding results for the case of functionalized 3WCNTs with 4 percent of the outer-wall nanotube sites being covalently functionalized are also displayed in Fig. 7(a). The results displayed in Fig. 7a can be summarized as follows:

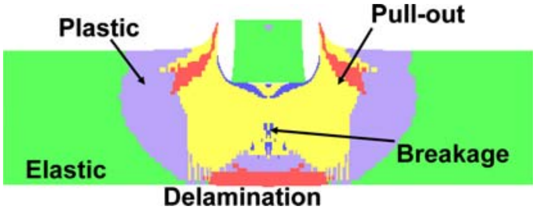

Fig. 6 An example of the results pertaining to the distribution of the material damage/failure modes resulting from the impact of a FSP with the 3WCNT-reinforced poly-vinyl-ester-epoxy composite armor

(a) Overall, the effect of reinforcement length/aspect ratio on the magnitude of kinetic energy fraction absorbed is small. At the reinforcement volume fraction of 0.1, the effect of reinforcement length is essentially insignificant. At the reinforcement volume fraction of 0.2, an increase in the reinforcement length gives rise to a decrease in the kinetic energy fraction absorbed, although the effect is quite small; and

(b) The magnitude of the reinforcement-length effect at different values of reinforcement volume fraction is not altered by the extent of covalent functionalization of the nanotubes’ outer-wall.

In order to help rationalize the results presented in Fig. 7a, the effect of the reinforcement aspect ratio on the in-plane stretching stiffness modulus and the out-of-plane shear modulus of the composite material at the same levels of the extent of covalent functionalization and the reinforcement volume fraction (used in Fig. 7a) is analyzed. The results of this analysis are presented in Fig. 7b and c, respectively. The in-plane stretching stiffness modulus relates the in-plane balanced tensile stresses with the corresponding tensile strains under a zero value of the through-the thickness stress and is defined as: $E_{\text{in}-\text{plane}} = \frac{(C_{11}+C_{12})C_{33}-2C_{13}^2}{C_{33}}$. The out-of-plane shear modulus is defined, on the other hand, as: $G_{\text{out-of-plane}} = C_{44}$. These elastic moduli quantify the stiffness of a composite plate with respect to in-plane stretching and through-the-thickness shear, the two modes of deformation which dominate the elastic interactions between an FSP and the armor.

The effect of reinforcement aspect ratio on the in-plane stretching stiffness modulus of the composite material at two levels (0% and 4%) of the extent of covalent functionalization of the nanotubes and at two levels (0.1 and 0.2) of the volume fraction of the nanotubes is displayed in Fig. 7b. The results displayed in Fig. 7b can be summarized as follows:

(a) The in-plane stretching stiffness modulus increases with the increase in the aspect ratio of the reinforcements at all levels of covalent functionalization and the reinforcement volume fractions examined;

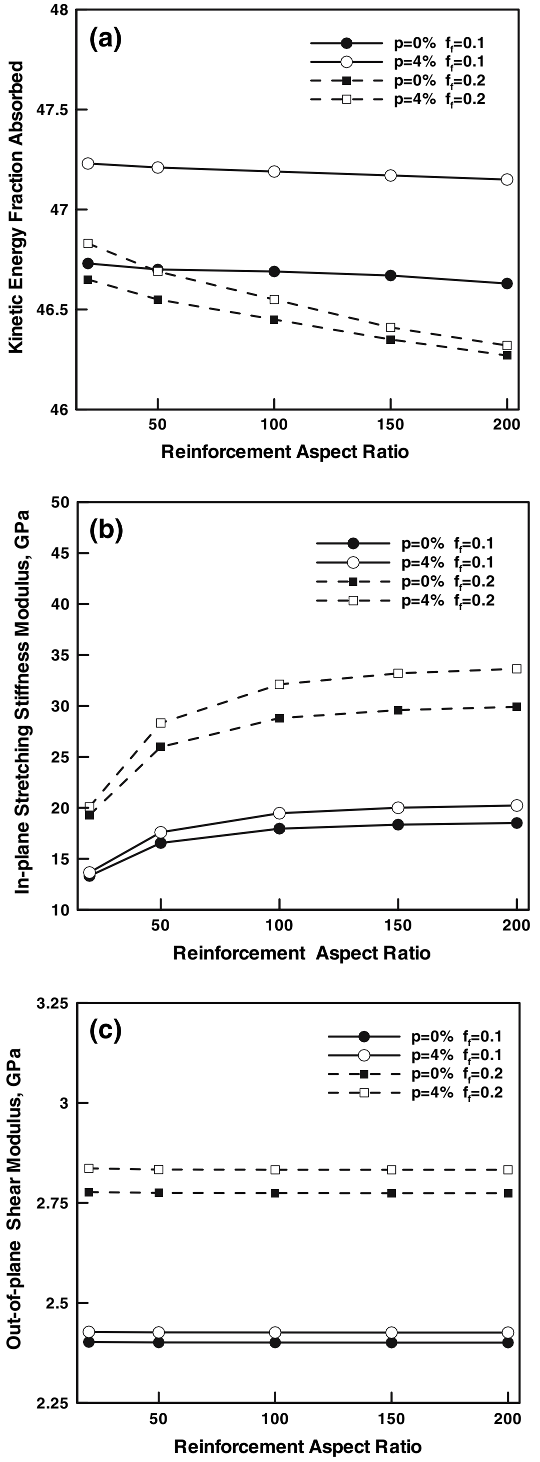

Fig. 7 The effect of the reinforcement aspect ratio on: (**a**) the kinetic energy fraction absorbed; (**b**) the in-plane stretching stiffness modulus, and (**c**) through-the-thickness shear modulus in 3WCNT-reinforced poly-vinyl-ester-epoxy composite

(b) The effect of an increase in the reinforcement aspect ratio is significant up to a value of approximately 100. Beyond this value of the aspect ratio, the effect is minor;

(c) At a constant value of the aspect ratio the in-plane stretching stiffness modulus increases with both the extent of covalent functionalization and with the reinforcement volume fraction, although the effect of the increased volume fraction is significantly higher; and

(d) At a fixed value of the reinforcement aspect ratio, the effect of covalent functionalization increases with an increase in the reinforcement volume fraction.

The results displayed in Fig. 7c reveal:

(a) The reinforcement aspect ratio has essentially a negligible effect on the out-of-plane shear modulus of the composite material; and

(b) At a fixed value of the aspect ratio, the out-of-plane shear modulus increases both with the reinforcement volume fraction and with the extent of covalent functionalization, although the effect of volume fraction is significantly higher.

Based on the findings reported above and an observation that no significant plastic deformation, fracture or erosion of the FSP occurs, it is clear that plastic deformation of the armor followed by damage and ultimate failure are the main mechanisms responsible for the observed absorption of the FSP's kinetic energy by the armor. Under such circumstances, the ability of the armor to absorb the kinetic energy is primarily controlled by the armor-material strength and toughness (two properties which are not affected by the reinforcement aspect ratio in the present material model). The effect of the armor-material stiffness is relatively weak and an increase in the material stiffness would decrease the kinetic energy fraction absorbed, as observed in Fig. 7a.

The effect of the 3WCNT volume fraction

As discussed in section ''Introduction,'' carbon nanotubes are quite expensive materials. Even the cost of MWCNTs produced using large-scale processing routes can run in to hundreds of dollars per pound. It is hence critical to examine the effect of the volume fraction of the carbon nanotubes on to the ballistic performance of armor in order to determine the optimal reinforcement volume fraction, i.e., the volume fraction beyond which the additional increase in armor's ballistic performance is not large enough to be justified by the high material cost. In this section, the effect of the 3WCNT volume fraction on the ballistic performance of the 3WNCT-reinforced poly-vinyl-ester-epoxy armor is examined. The volume of the 3WCNT reinforcements is computed by first approximating the 3WCNTs as an assembly of three concentric cylinders with the cylinders wall thickness equal to the inter-planar distance in graphite and then computing the total volume of the three cylinders.

The effect of reinforcement volume fraction in a range between 0.0125 and 0.5, on the kinetic energy fraction absorbed at two levels (0% and 4%) of the extent of covalent functionalization of the carbon nanotubes and two levels (20 and 200) of the reinforcement aspect ratio is shown in Fig. 8. The results shown in Fig. 8 can be summarized as follows:

(a) The effect of an increase in the reinforcement volume fraction on the kinetic energy fraction absorbed is relatively weak. Nevertheless, there appears to be an optimal volume fraction of the reinforcements. In the case of non-functionalized reinforcements the optimal reinforcement volume fraction is around 0.01–0.02. In the case of the reinforcements with the extent of covalent functionalization of 4% the optimal reinforcement volume fraction is around 0.1;

(b) While the effect of aspect ratio on the kinetic energy fraction absorbed is relatively small at low reinforcement volume fractions, the composite materials containing reinforcements with a low aspect ratio, has a higher capacity for kinetic energy absorption at higher values of reinforcement volume fraction; and

(c) The magnitude of the increase in the kinetic energy fraction absorbed associated with an increase in the extent of nanotube's outer-wall functionalization is a weak function of the reinforcement volume fraction.

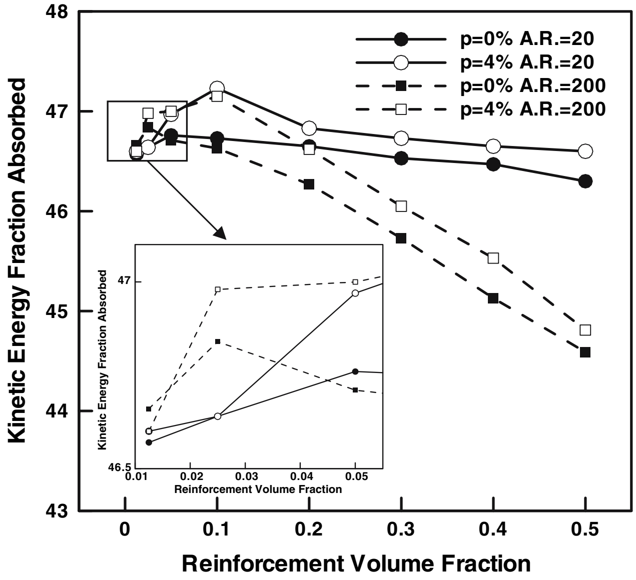

Fig. 8 The effect of the reinforcement volume fraction on the kinetic energy fraction absorbed in 3WCNT-reinforced poly-vinyl-ester-epoxy composite

These findings are also consistent with the fact that the ability of the composite material to absorb the kinetic energy of the FSP is dominated by the armor-material strength and toughness as discussed in the previous section.

The effect of the 3WCNT outer-wall covalent functionalization

As discussed in section ''Introduction,'' covalent functionalization of the outer walls of carbon-nanotube reinforcements plays a critical role in the matrix-to-reinforcement load transfer. A good matrix-to-reinforcement load transfer is very critical for composite materials used in structural (static load-bearing) applications. In conventional composite-material based armor, on the other hand, it is generally believed that a week matrix-to-reinforcement load transfer is preferred since it promotes a fiber pull-out mode of failure of the composite-material, the mode which is accompanied with substantial energy absorption. The primary energy absorption mechanism associated with the fiber pull-out is formation of the reinforcement and matrix free surfaces. This macroscopic-continuum view may not be fully applicable to the case of carbon-nanotube reinforced polymer-matrix composite in which the reinforcements are at the same length scale as the matrix molecules. A close look at the atomic-scale structure in the region surrounding the nanotube/polymer interface reveals that [32]: (a) There is no well-defined nanotube/polymer interface but rather an interfacial region (interphase) in which the polymer conformation is altered as a result of its interaction with the reinforcement; (b) During fiber pull-out, for the most part, no new free surfaces are created but rather the polymer confirmation and/or the reinforcement defect microstructure are changed; and (c) The matrix-to-reinforcement load transfer essentially ceases when the molecules of the polymer in the interphase region become disentangled from the bulk-polymer molecules and/or when the functionalizing bonds break. Under such conditions, the dominant energy absorption mechanism accompanying nanotube-reinforcement pull-out is the irreversible (plastic) deformation associated with the aforementioned molecule disentanglement. For this mechanism to be efficient, it should involve both high stress levels (promoted by a good matrix-to-reinforcement load transfer) and by a large interface strain prior to full disentanglement (affected by a competition between molecule disentanglement and detachment from the matrix, on one hand, and functionalizing-bond failure at he nanotube outer wall, on the other. As reported in section “Micro-mechanics based analysis of composite effective mechanical properties,” our atomistic simulation results [32] suggested that, at least initially, the fracture energy (and thus the strain preceding molecules disentanglement) increases with the extent of covalent side-wall functionalization of the 3WCNT reinforcements.

The effect of an increase in the extant of covalent functionalization of the nanotube’s outer-wall in a range between 0% and 8% on the kinetic energy fraction absorbed at two levels (20 and 200) of the reinforcement aspect ratio and two levels (0.1 and 0.2) of the reinforcement volume fraction is displayed in Fig. 9. The results shown in Fig. 9 indicate that:

(a) An increase in the extent of covalent functionalization gives rise to an increase in the kinetic energy fraction absorbed;
(b) This effect is relatively weak; and
(c) The magnitude of the effect of the extent of covalent functionalization is fairly insensitive to the magnitude of the reinforcement aspect ratio and/or the reinforcement volume fraction.

These results are consistent with those already reported and discussed in sections “The effect of the 3WCNT length/aspect ratio” and “The effect of the 3WCNT volume fraction” and with our previous findings [32] that the fracture energies increase with the extent of covalent functionalization and, hence, no further elaboration appears warranted.

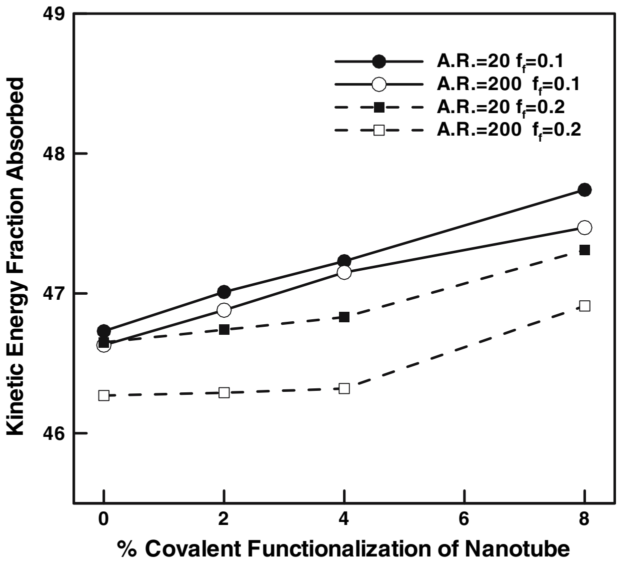

Fig. 9 The effect of the extent of nanotube-reinforcement side-wall covalent functionalization on the kinetic energy fraction absorbed in 3WCNT-reinforced poly-vinyl-ester-epoxy composite

Summary and conclusions

Based on the results obtained in the present work, the following summary and main conclusions can be made:

1. Atomic-scale calculation results obtained in our previous work [32] have been utilized within a micro-mechanics based framework to derive the continuum-level material model for a model multi-walled carbon nanotube-reinforced poly-vinyl-ester-epoxy matrix composite material.
2. The material model derived in the present work takes into account the effect of the major micro-structural aspects of the composite material, i.e., the reinforcements’ aspect ratio and volume fraction as well as the extent of covalent functionalization of the outer-wall of the nanotube-reinforcements.
3. The utilization of this model within a non-linear dynamics analysis of the interaction between a Fragment Simulated Projectile (FSP) and a carbon-nanotube reinforced polymer-matrix composite armor reveals that the dominant projectile-defeat mechanism is the absorption of the FSP’s kinetic energy. In other words, the composite material at hand appears to be primarily suitable as a spall liner in a multi-layer hybrid-armor structure.
4. The computational results obtained suggest that in order to maximize the ability of the composite armor to absorb the projectile’s kinetic energy, the armor composite material should contain around 10 volume percents of the reinforcements with a smaller aspect ratio (length) and a high level of covalent functionalization.

Acknowledgements The material presented in this paper is based on work supported by the Naval Research Office ender the Grant Number N00014-05-1-0844, by the U.S. Army/Clemson University Cooperative Agreement Number W911NF-04-2-0024 and by the U.S. Army Grant Number DAAD19-01-1-0661. The authors are indebted to Dr. Tom Juska of the Naval Research Laboratory and to Drs. Walter Roy, Bryan Cheeseman and Fred Stanton from the Army Research Laboratory.

References

1. Zhu J, Kim J, Peng H, Margrave JL, Khabashesku VN, Barrera EV (2003) Nano Lett 3:1107

2. Berber S, Kwon YK, Tomanek D (2000) Phys Rev Lett 84:4613
3. Lourie O, Wagner HD (1998) J Mater Res 13:2418
4. Walters DA, Ericson LM, Casavant MJ, Liu J, Colbert DT, Smith KA, Smalley RE (1999) Appl Phys Lett 74:3803
5. Andrews R, Jacques D, Rao AM, Rantell T, Derbyshire F, Chen Y, Chen J, Haddon RC (1999) Appl Phys Lett 75:1329
6. Mamedov AA, Kotov NA, Prato M, Guldi DM, Wicksted JP, Hirsch A (2002) Nat Mater 1:190
7. Salvetat JP, Briggs GAD, Bonard JM, Bacsa RR, Kulik AJ, Stockli T, Burnham NA, Forro L (1999) Phys Rev Lett 82:944
8. Chen J (2001) J Phys Chem B 105:2525
9. Frankland SJV, Caglar A, Brenner DW, Griebel M (2002) J Phys Chem B 106:3046
10. Watts PCP, Hsu WK, Chen GZ, Fray DJ, Kroto HW, Walton DRM (2001) J Mater Chem 11:2482
11. Kis A, Csanyi G, Salvetat J-P, Lee T-N, Couteau E, Kulik AJ, Benoit W, Brugger J, Forro L (2004) Nat Mater 3:153
12. Thess A (1996) Science 273:483
13. Dalton AB, Collins S, Munoz E, Razal JM, Ebron VH, Ferraris JP, Coleman JN, Kim BG, Baughman RH (2003) Nature 423:703
14. Zhu HW, Xu CL, Wu DH, Wei BQ, Vajtai R, Ajayan PM (2002) Science 296:884
15. Ausman KD, Piner R, Lourie O, Rouff RS, Korobov M (2000) J Phys Chem B 104:8911
16. Shaffer MS, Windle AH (1999) Adv Mater 11:937
17. Qian D, Dickey EC, Andrews R, Rantell T (2000) Appl Phys Lett 76:2868
18. Qian D, Dickey EC (2001) J Microsc 204:39
19. Grimes CA, Dickey EC, Mungle C, Ong KG, Qian D (2001) J Appl Phys 90:4134
20. Safadi B, Andrews R, Grulke EA (2002) J Appl Polym Sci 84:2660
21. Pirlot C, Willems I, Fonseca A, Nagy JB, Delhalle J (2002) Adv Eng Mater 4:109
22. Andrews R, Jacques D, Minot M, Randell T (2002) Macromol Mater Eng 287:395
23. Potschke P, Fornes TD, Paul DR (2002) Polymer 43:3247
24. Gong X, Liu J, Baskaran S, Voise RD, Young JS (2000) Chem Mater 12:1049
25. Star A, Stoddart JF, Steuerman MD, Boukai A, Wong EW, Yang X, Chung S, Choi H, Heath JR (2001) Angew Chem Int Edn Engl 40:1721
26. Viswanathan G, Chakrapani N, Yang H, Wei B, Chung H, Cho K, Ryu CY, Ajayan PM (2003) J Am Chem Soc 125:9258
27. Wu W, Zhang S, Li Y, Li J, Liu L, Qin Y, Guo ZX, Dai L, Ye C, Zhu DB (2003) Macromolecules 36:6286
28. Penumadu D, Dutta A, Pharr GM, Files B (2003) J Mater Res 18:1849
29. Dutta AK, Penumadu D, Files B (2004) J Mater Res 19:158
30. Grujicic M, Cao G, Roy WN (2004) Appl Surf Sci 227:349
31. Grujicic M, Cao G, Roy WN (2004) J Mater Sci 39:2315
32. Grujicic M, Sun Y-P, Koudela KL (2006) Appl Surf Sci (accepted for publication, March)
33. Grujicic M (2006) Unpublished work. Clemson University
34. Ashby MF (1992) Material selection in mechanical design, 3rd edn. Butterworth-Heinemann Oxford, United Kingdom
35. Haque A, Hossain MK (2003) J Compos Mater 37:647
36. Mori T, Tanaka K (1973) Acta Metall 21:571
37. Mura T (1982) Micromechanics of defects in solids. Martinus Nijhoff, The Hague
38. Qui YP, Weng GJ (1990) Inter J Eng Sci 28:1121
39. Benveniste Y (1987) Mech Mater 6:147
40. Eshelby JD (1957) Proc R Soc London Ser A 241A:376
41. Odegard GM, Gates TS, Wise KE, Park C, Siochi EJ (2003) Compos Sci Technol 63:1671
42. Gruneisen E (1926) Handbuch der Physik. Springer-Verlag, Berlin
43. AUTODYN-2D and 3D, Version 6.1. (2006) User documentation. Century Dynamics Inc
44. Pandurangan B (2006) Ph.D. work in progress. Clemson University, April 2006